JOURNAL OF MATERIALS SCIENCE **32** (1997) 4645–4654

The complex characteristics of crystallization of the $Fe_{75}Si_{15}B_{10}$ glassy ribbon

EMÍLIA ILLEKOVÁ; I. MAT'KO; P. DUHAJ
Institute of Physics, SAS, Dúbravská cesta 9, 842 28 Bratislava, Slovak Republic
FRANCE-ANNE KUHNAST
Laboratoire de Thermodynamique Métallurgique, Université de Nancy I, BP 239, 54506 Vandoeuvre-lès-Nancy Cédex, France

The $Fe_{75}Si_{15}B_{10}$ glassy ribbon was examined in the course of various isothermal and dynamic heat treatments. The number, type and mechanism of formation of the crystallization products formed during two crystallization stages in this alloy were determined by differential scanning calorimetry (DSC), thermomagnetometry, transmission electron microscopy and X-ray diffraction measurements. It is concluded that the first DSC peak is due to the crystallization of α-Fe(Si) or Fe_3Si and the composite microcrystals containing Fe_3B cores with α-Fe(Si) envelopes. The metastable Fe_3B subsequently transforms into the stable Fe_2B in the second DSC peak. The remaining amorphous matrix crystallizes by the eutectic reaction also in the second DSC peak forming the Fe_3Si and Fe_2B eutectic structures. The apparent activation energy E_1^* decreases during the first crystallization stage from 480 kJ (g atom^{-1}), characteristic of the Johnson–Mehl–Avrami (JMA) nucleation-and-growth kinetics of the as-quenched sample, to 350 kJ (g atom)$^{-1}$ implying a dominance of the diffusion-controlled growth of iron in the already pre-nucleated sample. Simultaneously, the JMA exponent n_1 decreases from 2.5 to 1.5. The apparent activation energy E_2^* depends on the temperature of the first crystallization stage. It decreases with increasing T_a from 384 to 282 kJ (g atom)$^{-1}$. This phenomenon was attributed to modification of the chemical composition of the remaining eutectic after the temperature dependent primary crystallization of Fe_3B within the composites. The value of n_2 is 3.

1. Introduction

The Fe–Si–B based metallic glasses produced by melt spinning have been the object of much scientific and technological attention during the last fifteen years, particularly because of their soft magnetic properties which are comparable to or better than those of conventional crystalline materials [1, 2]. As these properties are affected by the crystallization, the thermal stability of metallic glasses has been studied extensively. However, the transition mechanism from the amorphous to the crystalline state, in the case of the Fe–Si–B glasses, is particularly complicated [3–7]. The crystallization kinetics, as in the case of all the Fe–B-based glasses, is strongly dependent on the chemical composition. The dynamic DSC traces usually show two more or less overlapping exothermal reactions, the second one representing the crystallization of the pseudobinary eutectics and the first one the crystallization of the excess concentrations of components of the alloy to modify the remaining amorphous matrix to reach the chemical composition of the pseudobinary eutectic. The crystallized alloy contains several phases in both metastable and stable crystalline states depending on the heat treatment conditions. Therefore it is necessary to control the heat treatment conditions precisely to understand the crystallization process in detail.

Gibson and Delamore [3–5] studied the mechanism of crystallization of $Fe_{96-x}Si_4B_x$ glassy ribbons in the range 14–22 at % B and $Fe_{90-x}Si_{10}B_x$ glassy ribbons in the range 10–18 at % B by the use of transmission electron microscopy (TEM). In the papers of Illeková [6], Illeková *et al.* [7] and Mat'ko *et al.* [8] the kinetics of the crystallization of $Fe_{80-x}Si_xB_{20}$ glassy ribbons in the range of 2–10 at % Si was investigated using dynamic and isothermal DSC measurements. All these results indicate that the types of Fe–Si–B crystallization products and the kinetics of the two crystallization steps are related to the position of the alloy composition with respect to the pseudobinary eutectic trough. Generally, this eutectic trough separates the hypoeutectic Fe-Si-B alloys (with high Fe content), crystallizing first to α-Fe(Si), from the hypereutectic ones where Fe_3B crystallization is the primary transformation.

In this paper, the crystallization of the $Fe_{75}Si_{15}B_{10}$ glassy ribbon is studied. The chemical composition of this metallic glass lies very close to the pseudobinary eutectic trough [9] having higher Si content than the previously referred materials. The complex isothermal and linear heating DSC measurements and combined Kissinger [10], isoconversional [6] and Suriñach [11, 6] kinetic procedures are used. Previously [12], we reported on the influence of pre-annealing on the dynamic DSC kinetic parameters of the crystallization for this metallic glass. In the present paper, the problem of the complex relation between the isothermal and the dynamic DSC kinetic studies is discussed. Also, using thermomagnetometry (TM), X-ray diffraction and TEM measurements, the originating crystalline phases, their morphology and transformation mechanisms are studied to verify the DSC results.

This study is part of a complex investigation of the thermodynamic stability of the Fe–Si–B based metallic glass ribbons [6–8, 12, 13].

2. Experimental procedure

The master alloys were prepared from the constituent elements of at least 99.5% purity. The $Fe_{75}Si_{15}B_{10}$ glassy ribbons, 10 mm wide and 30 µm thick, were prepared by the planar-flow casting method. Chemical analysis of the ribbons was performed by inductively coupled plasma spectroscopy. The amorphous state of the samples was checked using X-ray analysis.

The thermal measurements on the as-quenched samples, (mass ~6 mg and cut into small pieces, placed in an Al sample pan and covered with an Al lid), were performed in a Perkin-Elmer DSC7 instrument using an empty pan as reference. A N_2 gas flow was used for the ambient atmosphere. Both a dynamic measuring regime, with constant heating rates, ϕ, of 10–60 K min^{-1}, and an isothermal measuring regime at annealing temperatures, T_a, from 768 K to 808 K (with a heating ramp, ϕ, of 40 K min^{-1}) were used. Cooling at the highest rate of -200 K min^{-1} always followed the measuring run.

The temperature dependence of the magnetic force (TM) of the square-shaped ~0.4 mg heavy samples of the as-quenched and crystallized metallic ribbons was measured with a Perkin-Elmer thermomagnetometer a TGA1 thermobalance equipped with a permanent magnet (19 mT). The measuring regime was equivalent to the DSC dynamic regime with $\phi =$ 40 K min^{-1}. An argon gas flow atmosphere was used.

The absolute temperature (error less than 0.05%) and the enthalpy (error less than 2%) of the DSC and TM instruments were calibrated with the melting points of indium and zinc standards and the Curie transformations of the alumel, nickel, percaloy and iron standards, respectively, for all heating rates. Furthermore no heating rate influence on the Curie point of nickel was observed.

The standard discs of 3 mm diameter for electron microscopy were cut from the as-quenched ribbons. After the corresponding heat treatment in the DSC apparatus the discs were thinned by ion beam milling. Transmission electron microscopy and electron diffraction were performed using a JEM 1200 EX electron microscope.

The samples for X-ray analysis were annealed in a vacuum furnace at a pressure of 10^{-3} Pa. The X-ray measurements were performed using CuK_α radiation and a graphite monochromator in the diffracted beam.

3. Results

3.1. Differential scanning calorimetry and thermomagnetometry

The samples of the $Fe_{75}Si_{15}B_{10}$ glassy ribbon were studied by conventional DSC and TM. In Fig. 1 the variation of the rate of the enthalpy change with temperature is plotted as the full line for the as-quenched sample. The large shallow structural relaxation exotherm, small sharp endothermic anomaly due to the Curie point and the two-stage exothermic crystallization with a high temperature tail are evident on the DSC curve. None of these anomalies was reproduced in the subsequent measuring run on the crystallized samples. The dotted and dashed lines in Fig. 1 are the TM curves proportional to the temperature dependence of the magnetization which monitor, in this way, the magnetic power of the as-quenched and crystallized samples. The heating rate, ϕ, was always 40 K min^{-1}. All dependencies confirm the loss of ferromagnetism of the amorphous matrix at the Curie temperature $T_{c,a} = 700.9$ K. On the contrary, the ferromagnetism of the sample increases steeply during the two-stage crystallization reaction. The TM curve of the completely crystallized sample (dashed line in Fig. 1), revealing the presence of several ferromagnetic phases, shows a distribution of the Curie temperatures with two maxima at ~867 K and ~1015 K. (The Curie points of the Fe_3B, Fe_3Si, Fe_2B and α-Fe(Si) phases are 800 K, 840 K, 1015 K and between 840 and 1043 K, depending on the content of Si [14], respectively.)

Two large overlapping exothermic reactions related to the two different phase transformations were observed on the dynamic DSC curve (full line in Fig. 1 and Fig. 2) during the crystallization of the sample. The lower temperature peak (hereafter referred to as the first reaction, R1) starts at the temperature $T_{x1} = 817.4$ K and has a maximum at $T_{p1} =$ 830.7 K. The higher temperature peak (hereafter referred to as the second reaction, R2) starts before the end of the first one and has a maximum at $T_{p2} = 848.4$ K. The transformation enthalpies of R1 and R2 estimated from the integrated intensities of the dynamic DSC peaks are 103.9 and 6.6 J g^{-1}, respectively (all at $\phi = 40$ K min^{-1}). The overlap, the relation between the enthalpies and also the kinetics of the R1 and R2 reactions depend both on the heating rate and the pre-annealing of the sample. Generally, any heat treatment of a sample at temperatures T_a close to T_{x1} for which $T_{x1} - 50\text{ K} \leqslant T_a \leqslant T_{x1}$ starts the R1 reaction. The annealing shifts both crystallization exotherms to lower temperatures, diminishing the enthalpy and also the Johnson–Mehl–Avrami exponent of R1. Fig. 2 illustrates the dynamic DSC curves for the sample pre-annealed at $T_a = 793$ K for different pre-annealing times, t_a, (which characterize the degree of

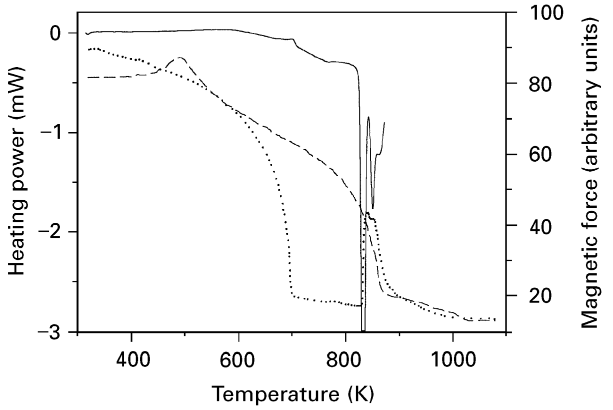

Figure 1 DSC and thermomagnetometry linear-heating curves of the $Fe_{75}Si_{15}B_{10}$ ribbon. (——) The DSC curve (minus the first and second runs) of the as-quenched glassy sample, (......) and (- - - -) the TM curves of the as-quenched glassy and completely crystalline samples. Heating rate 40 K min^{-1}.

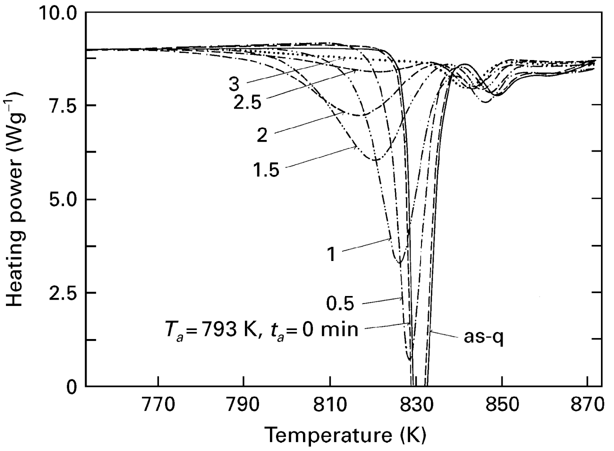

Figure 2 The effect of pre-annealing on the linear-heating DSC curve (minus first and second runs) of the crystallization of the glassy $Fe_{75}Si_{15}B_{10}$ ribbon (the pre-annealing temperature $T_a = 793$ K, the pre-annealing time t_a being the parameter). Heating rate 40 K min^{-1}.

crystallization) heated at $\phi = 40\ \mathrm{K\,min}^{-1}$. We reported on the details of the pre-annealing influence on the kinetics of the crystallization of the $Fe_{75}Si_{15}B_{10}$ glassy ribbon estimated from the dynamic DSC measurements in [12].

A series of isothermal DSC experiments was carried out on the as-quenched ribbons at temperatures T_a in the range 768–808 K close to T_{x1}. After the incubation time, two overlapping exothermic peaks, R1 and R2, were always observed (Fig. 3). None of these anomalies was reproduced in the subsequent isothermal or dynamic measuring run. The incubation times, τ, the times of the peak maxima, t_m, and times of the peak ends, t_e, for R1 and R2 are $\tau_1 = 1.00$ min, $t_{m1} = 2.34$ min, $t_{e1} = 5.37$ min and $\tau_2 = 5.37$ min, $t_{m2} = 6.55$ min and $t_{e2} = 9.55$ min (all at $T_a = 793$ K), respectively. These times are indicative of an Arrhenius temperature dependence. The enthalpies of the first and second peaks, ΔH_1 and ΔH_2, derived from the areas of the DSC curves, are 102.0 and 6.7 J g^{-1} (at $T_a = 798$ K), respectively. ΔH_1 increases at the expense of ΔH_2 with increasing T_a. The absolute values agree well with those estimated from the dynamic DSC measurements. This means that the same transformations take place in both experiments.

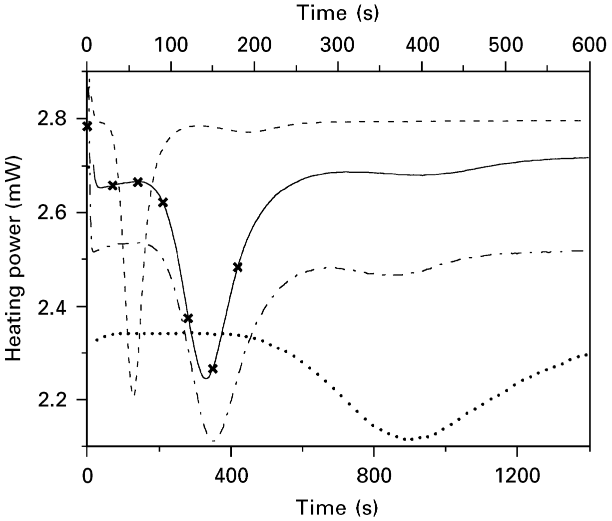

Figure 3 Isothermal DSC crystallization curves (minus first and second runs) at various temperatures T_a of the as-quenched glassy $Fe_{75}Si_{15}B_{10}$ ribbon. For $T_a = 803$ K (-----) and 793 K (——) the upper time scale holds. For $T_a = 783$ K (– . – . –) and 773 K (......) the lower time scale holds. The symbols (×) mark the partial crystallization effects produced by the pre-annealing heat treatments for the measurements shown in Figs 2 and 13.

3.2. Kinetic analysis

Both in the dynamic and isothermal DSC measurements the quasi-linear temperature dependences in the second measuring runs were measured (excepting transient instrument effects which were similar to those of the first measuring runs). Therefore, we extracted the kinetic information from the temperature and time dependences of the specific heat of the sample by subtraction of the first and second measuring runs.

In our kinetic studies, we assumed the R1 and R2 crystallization steps to be mutually independent and therefore the kinetic equations were applied to each step separately. The straight line connecting the first and the last point of a DSC peak was used as the baseline for the $\Delta H(T, t)$ and $\alpha(T, t) = \Delta H(T, t)/\Delta H$ calculations. ΔH and $\Delta H(T, t)$ are the total and partial integrals of the measured DSC signals, namely dH/dT or dH/dt. $\alpha(T, t)$ is the fraction already transformed at the temperature T and in the time t (degree of transformation).

Generally, in the case of the dynamic measuring regime, the kinetics of any thermally activated phase transformation must be dependent on the heating rate ϕ. Kissinger [10] has found a simple relation between ϕ and the temperature of the maximum rate of transformation (which in the case of DSC is T_p) in the case of a single process. The slope of the $\ln[\phi/T_p^2]$ versus $1/T_p$ linear plot is the activation energy of the process, E_K^*. The observed Kissinger plots of the two crystallization transformations in the as-quenched $Fe_{75}Si_{15}B_{10}$ are shown in Fig. 4. All data points for the R1 peak fall on a straight line with a calculated

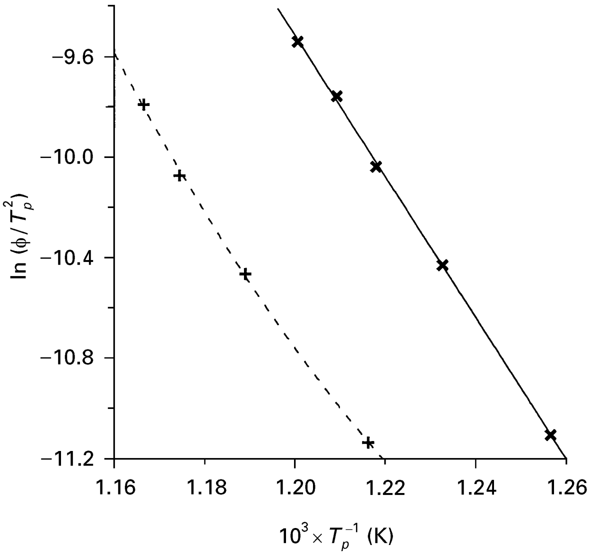

Figure 4 The Kissinger plots of the heating rate shift in the DSC peak temperature for the as-quenched glassy $Fe_{75}Si_{15}B_{10}$ ribbon. The activation energies (E_K^*) for the R1 (×) and R2 (+) peak are estimated as 473 ± 12.9 and 395 ± 14.3 kJ (g atom)$^{-1}$, respectively.

activation energy, E_{K1}^*, of 473 ±13 kJ (g atom)$^{-1}$. However, a temperature dependent slope revealing some peculiarities in the transformation with an average activation energy, E_{K2}^*, of 395 ±14 kJ (g atom)$^{-1}$ is observed in the case of R2.

In the case of our isothermal measurements, the Arrhenius temperature dependence

$$\theta = \theta_0 \exp[E_\theta^*/RT] \qquad (1)$$

for the measured incubation times and the times of the maxima and ends of both R1 and R2 peaks has already been mentioned above. θ_0 and E_θ^* are constants and R is the gas constant. This suggests the validity of the Johnson–Mehl–Avrami nucleation-and-growth (JMA) kinetic law for the time dependence of the degree of transformation

$$\alpha(t) = 1 - \exp\{-[k(T)t]^n\} \qquad (2)$$

The Arrhenius temperature dependence follows the definition of the rate constant

$$k(T) = A\exp[-E_{JMA}^*/RT] \qquad (3)$$

A, E_{JMA}^* and n are the JMA model parameters, namely the pre-exponential factor, the apparent activation energy and the exponent, respectively, also for the investigated R1 and R2 transformations.

If α is constant, Equation 2 yields

$$k(T)t(\alpha) = \text{const} \qquad (4)$$

independent of T. In addition, the condition for the maximum isothermal transformation rate $d^2\alpha/dt^2|_m = 0$ is

$$\alpha_m = 1 - \exp[(1-n)/n], \qquad (5)$$

which is independent of T. Because, by definition, $\alpha(\tau) = 0$, $\alpha(t_e) = 1$ and, on the basis of Equation 5, also $\alpha(t_m) = \text{const}$, Equation 4 can be rewritten to Equation 1 for τ, t_m and t_e. Various activation energies $E_{\tau_1}^* = 651$ ±67 kJ (g atom)$^{-1}$, $E_{t_{m1}}^* = 480$ ±5 kJ (g atom)$^{-1}$ and $E_{\tau_2}^* = 417$ ±3 kJ (g atom)$^{-1}$, $E_{t_{m2}}^* = 386$ ±1 kJ (g atom)$^{-1}$ and $E_{t_{e2}}^* = 363$ ±11 kJ (g atom)$^{-1}$ depending on the times τ_1, t_{m1}, τ_2, t_{m2} and t_{e2} for the R1 and R2 crystallization stages of the as-quenched $Fe_{75}Si_{15}B_{10}$ glassy ribbon were found. Neither the end of the R1 stage, the time t_{e1}, nor the activation energy $E_{t_{e1}}^*$ were determined because of the overlap of the R1 and R2 peaks in the isothermal DSC measurements (see, e.g. Fig. 3).

The monitoring of the evolution of the effective activation energy of the transformation, $E^*(\alpha)$, with the proceeding transformation, characterized by α, is based on the isothermal isoconversional method [6]. Taking Equation 4, the logarithm of the time derivation of Equation 2 is

$$\ln(d\alpha/dt)|_\alpha = \text{const} - E^*(\alpha)/(RT_a) \qquad (6)$$

$d\alpha/dt$ is directly proportional to the DSC isothermal signal ($d\alpha/dt = (1/\Delta H)(dH/dt)$). The measured DSC isothermal signals at the times $t_{\alpha 1}$ and $t_{\alpha 2}$, corresponding to the same α (increasing from 0.1 to 0.9 in steps of 0.1), versus $1/T_a$ fall on straight lines, the slopes of which give $E_1^*(\alpha)$ and $E_2^*(\alpha)$ for the R1 and R2 peaks, respectively. Both activation energies as functions of the degree of transformation are shown in Fig. 5. $E_1^*(\alpha)$ decreases monotonically as the R1 transformation proceeds for $\alpha_1 > 0.6$. We have found a similar $E_1^*(\alpha)$ dependence also from the dynamic DSC measurements by the use of the linear-heating isoconversional method (Fig. 9 in [12]). $E_2^*(\alpha)$ remains constant during the whole R2 transformation within the uncertainities of the calculated energies. Its irregular absolute value will be discussed later.

In order to test whether our choice of the JMA nucleation-and-growth kinetics is relevant also for the studied R1 and R2 crystallization stages of the as-quenched $Fe_{75}Si_{15}B_{10}$ ribbon, the Suriñach curve fitting procedure [11, 6] was used. In this way, each single DSC curve (isothermal or dynamic), represented in an appropriate coordination system, namely, $\ln[d\alpha(T,t)/dt] + E^*/(RT_a)$ or $\ln[d\alpha(T,t)/dT] + E^*/[RT(t)] + \ln\phi$ versus $-\ln[1-\alpha(T,t)]$, is compared

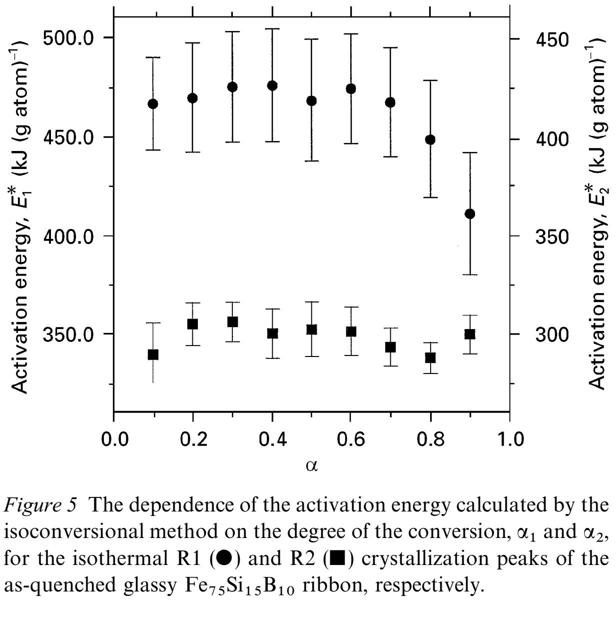

Figure 5 The dependence of the activation energy calculated by the isoconversional method on the degree of the conversion, α_1 and α_2, for the isothermal R1 (●) and R2 (■) crystallization peaks of the as-quenched glassy $Fe_{75}Si_{15}B_{10}$ ribbon, respectively.

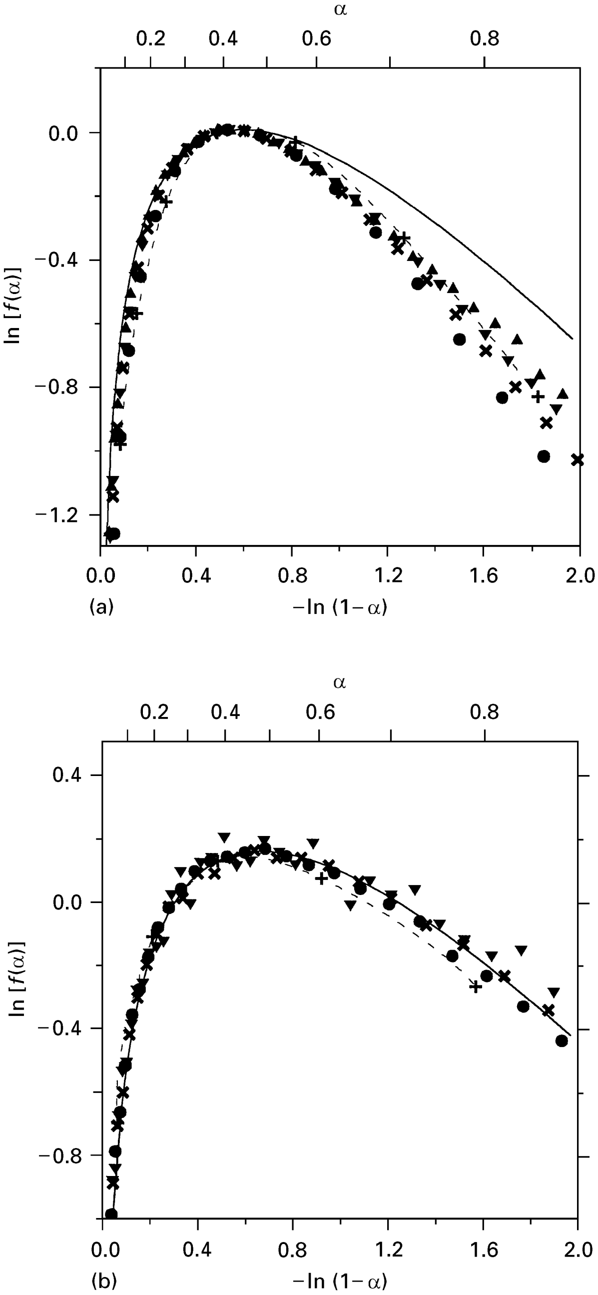

Figure 6 (a) and (b): the Suriñach plots [11] for R1 and R2, respectively, both for the isothermal and linear-heating crystallization peaks of the as-quenched glassy $Fe_{75}Si_{15}B_{10}$ ribbon and the theoretical curves obtained for the JMA kinetic equation with the exponents $n_1 = 2.5$ in the case of R1 and $n_2 = 3$ in the case of R2, respectively. Full lines are the theoretical curves. Symbols are the experimental data for the isotherm at $T_a = 773$ K (▲), 783 K (▼), 793 K (×), 808 K (●); and the linear-heating at $\phi = 40\ \mathrm{K\,min^{-1}}$ (+) (the connecting dashed line is a guide to the eye for + symbols).

with the theoretically modelled ones. All measured DSC curves were used. All measured data for both crystallization stages can be unambiguously characterized by the JMA nucleation-and-growth kinetics (Figs 6a and b). In the case of R1, all Suriñach graphs follow one master curve, the value of its JMA exponent, n_1, is not constant. In the early stages, n_1 changes steeply revealing the transient nucleation effect to reach the value of $n_1 = 2.5$ in the central part of the transformation ($0.25 < \alpha_1 < 0.55$). Later in the transformation n_1 continuously decreases reflecting the probable saturation of nucleation (and in the case of the dynamic measurements also the influence of the second crystallization step). The rate of this nucleation decay increases with increasing temperature. In the case of R2, the transformation can well be characterized by the single JMA nucleation-and-growth kinetic law with the JMA exponent $n_2 = 3$. Moreover, because the vertical shift between the simplified $\ln[d\alpha(T_a, t)/dt]$ versus $-\ln[1 - \alpha(T_a, t)]$ representation of any two isothermal measurements is proportional to E^* [6], the temperature dependence of both activation energies can be tested. $E_1^* = 484 \pm 3$ kJ (g atom)$^{-1}$, independent of T_a, and E_2^* decreasing from 384 to 293 kJ (g atom)$^{-1}$ with increasing T_a were found.

3.3. Transmission electron microscopy and X-ray diffraction

The results of TEM and X-ray analysis of the crystallization process for $Fe_{75}Si_{15}B_{10}$ glassy ribbon are in agreement with our other results [8] for the whole Fe–Si–B system and reveal its considerable complexity from the structural point of view.

TEM indicates the nucleation and growth of two types of crystals during the first reaction. The first type are the supersaturated α-Fe(Si) and Fe_3Si crystals having a dendritic morphology (Fig. 7). The second type are the crystals of the metastable orthorhombic Fe_3B having a shape of prolate ellipsoids, which are frequently faulted (Fig. 8). At the surfaces of these crystals the α-Fe(Si) phase, forming so-called composite crystals, heterogeneously nucleates and grows. The structure of these composites was confirmed using a tilting device and dark field image analysis (Figs 9a and b). Although there is no evidence in our TEM experimental data for the presence of the Fe_3Si phase in these regions, it could not be completely excluded. The metastable Fe_3B transforms into the stable tetragonal Fe_2B phase and α-Fe by a eutectic decomposition reaction during the second stage of the crystallization. Any remaining surrounding amorphous matrix also crystallizes into Fe_3Si and Fe_2B by a eutectic reaction during the R2 stage.

X-ray diffraction analysis requires annealing of the investigated material in the best vacuum possible. The preparation of the material in a vacuum furnace and the mass of the samples does not allow the observation of the initial stage of the first reaction (as is the case for heat treatment of the samples using DSC) without a considerable shift of temperature. Using this method, the samples annealed for 5 min at 793 K and 60 min at 823 K were examined, the former corresponding to the progressed R1 reaction stage and the latter corresponding to the completely crystallized sample. The X-ray diffraction pattern of the first sample (Fig. 10) indicates the presence of the supersaturated α-Fe(Si), Fe_3Si and the orthorhombic Fe_3B phase, which is in agreement with the TEM observations. The positions of the α-Fe(Si) peaks correspond to a lattice parameter of ~0.284 nm, according to which the content of the silicon is estimated to be approximately 20 at %. The diffraction pattern of the

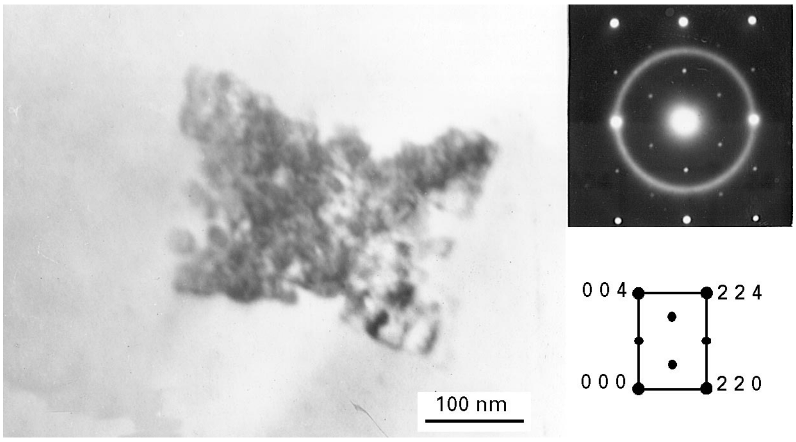

Figure 7 TEM image taken from the sample of the glassy $Fe_{75}Si_{15}B_{10}$ ribbon. Pre-annealing temperature $T_a = 793$ K, pre-annealing time $t_a = 1.5$ min. Magnification 180 000 ×. In the upper-right corner: the selected-area electron diffraction pattern from the imaged crystal, in the lower-right corner: its indexing for the Fe_3Si structure.

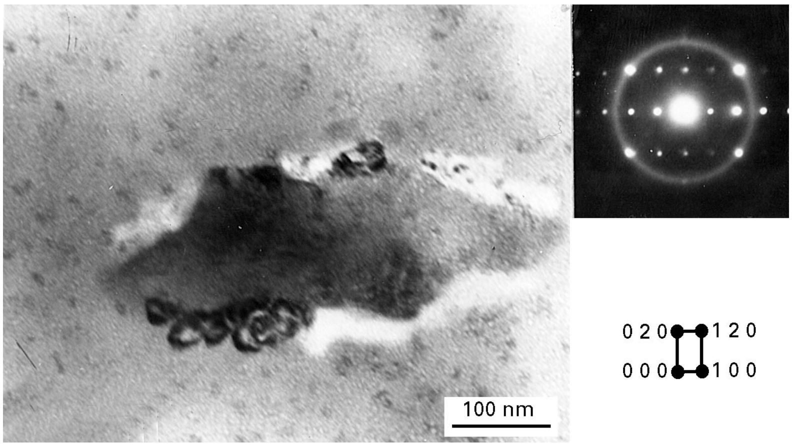

Figure 8 TEM image taken from the same sample as in Fig. 7. In the upper-right corner: selected-area electron diffraction pattern from the imaged crystal, in the lower-right corner: its indexing for the Fe_3B structure.

second sample (Fig. 10) reveals the presence of the α-Fe(Si) and Fe_3Si phases and, in contrast to the first sample, only the stable tetragonal Fe_2B phase. In addition, the α-Fe(Si) diffraction peaks are shifted slightly to higher 2ϑ angles, indicating a progressive enrichment in Si of the α-Fe(Si) solid solution and/or a relative increase of the amount of Fe_3Si at the expense of α-Fe(Si). These results prove the existence of a transformation reaction of the metastable boride to the stable boride running simultaneously with the crystallization of the pseudobinary eutectics during the R2 stage.

4. Interpretation

4.1. Activation energies and Avrami exponents

The activation energies of the R1 and R2 crystallization stages in the $Fe_{75}Si_{15}B_{10}$ ribbon were determined on the basis of both dynamic and isothermal DSC measurements described in the previous paragraphs and in [12]. As is often observed in the case of the crystallization of metallic glasses, including our samples, the determined activation energies are dependent on the measuring regime and the kinetic analysis method used. These quantities are summarized in Figs 11 and 12. It can be seen, that they agree within the experimental errors for both R1 and R2 stages. Nevertheless, on the basis of these absolute values and their error bars, several dependences can be observed and several conclusions formulated.

In the case of R1, a systematic decrease of $E_1^*(\alpha)$ with the proceeding transformation both in the isothermal (Fig. 5) and dynamic (Fig. 9 in [12]) temperature regimes was observed for $\alpha > 0.6$. Therefore the quantities determinated on the basis of the temperature dependencies of the isothermal transformation times (Equation 1) are also dependent on the times θ for which the fittings were performed.

Moreover, the $n_1(\alpha)$ dependence was extracted from the Suriñach fitting of both isothermal and dynamic DSC measurements (Fig. 6a and Fig. 10a in [12]). $n_1(\alpha)$, after exhibiting the transient nucleation effects at the beginning of the R1 transformation, stabilizes at $n_1 = 2.5$. Later, the decrease of $E_1^*(\alpha)$ (Fig. 5) is accompanied by a decrease in n_1 to a value of 1.5.

On the other hand, the Kissinger analysis of the dynamic results (Fig. 4) and the Suriñach fittings of the individual isothermal DSC records showed no temperature dependence, $E_1^* \neq f(T)$, in the case of the R1

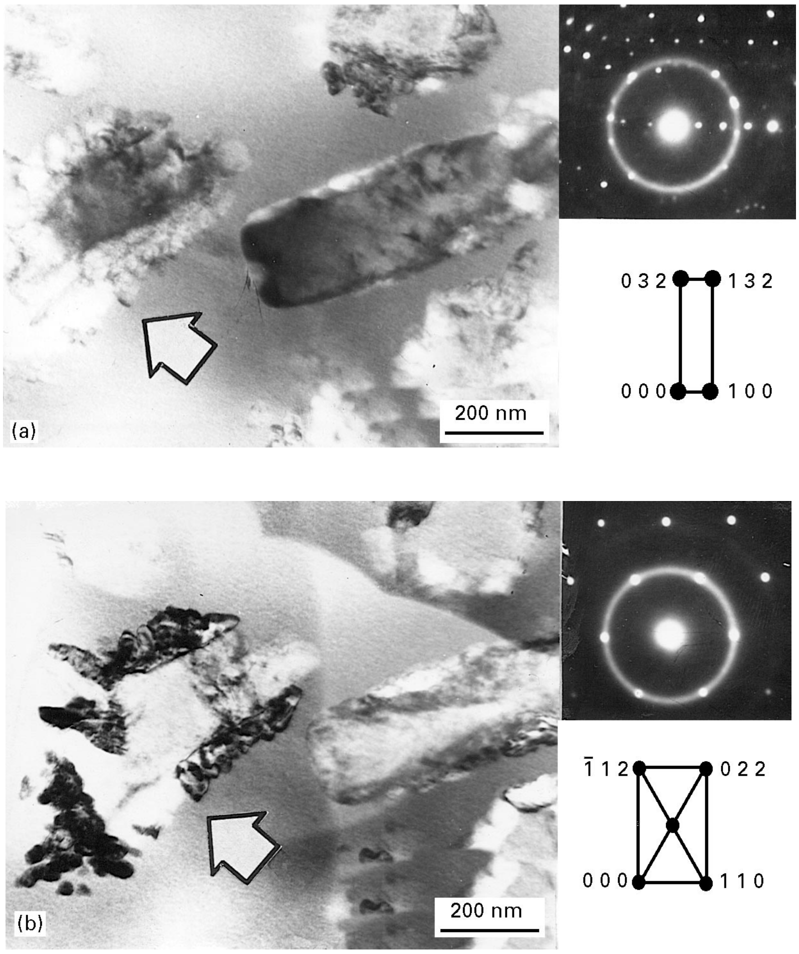

Figure 9 (a) TEM image taken from the sample of the $Fe_{75}Si_{15}B_{10}$ glassy ribbon. Pre-annealing temperature $T_a = 793$ K, pre-annealing time $t_a = 2$ min. Magnification 120 000 ×. In the upper-right corner: selected-area electron diffraction pattern from the marked crystal, in the lower-right corner: its indexing for the composite Fe_3B structure; (b) TEM image taken from the same sample as above but at another orientation with respect to the primary beam. In the upper-right corner: selected-area electron diffraction pattern from the marked crystal (same as above), in the lower-right corner: its indexing for the α-Fe(Si) structure.

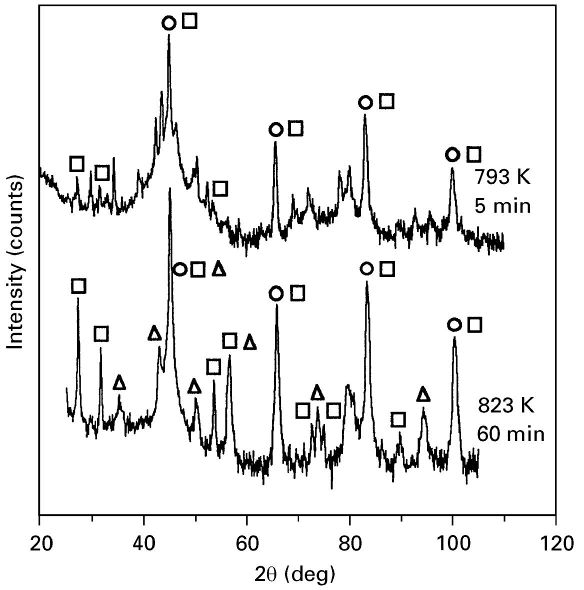

Figure 10 X-ray diffraction spectra taken from the $Fe_{75}Si_{15}B_{10}$ glassy ribbon: annealed 5 min at 793 K and 60 min at 823 K. Peak description: ○ – α-Fe(Si), □ – Fe_3Si, △ – Fe_2B. Most of the remaining peaks of the upper diagram can be ascribed to Fe_3B.

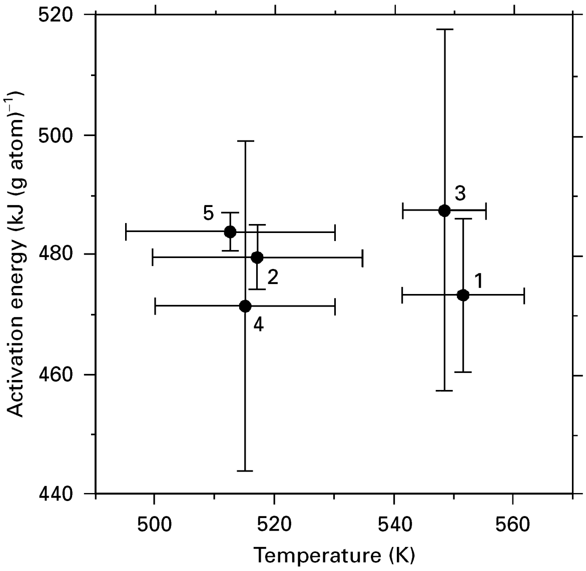

Figure 11 The dependence of the activation energy result on the method of DSC kinetic analysis used for the first crystallization stage, R1, in the as-quenched $Fe_{75}Si_{15}B_{10}$ glassy ribbon. (1) The Kissinger activation energy, E^*_K, (2) the activation energy calculated from the temperature dependence of the isothermal peak maximum time, E^*_{tm}, (3) and (4) the isoconversional linear-heating and isothermal activation energy, E^*_{Tch} and E^*_{Ti}, respectively, (5) the isothermal Suriñach method activation energy, E^*_S. Horizontal bars – the width of the temperature interval taken into account; vertical bars – the error of the presented mean value.

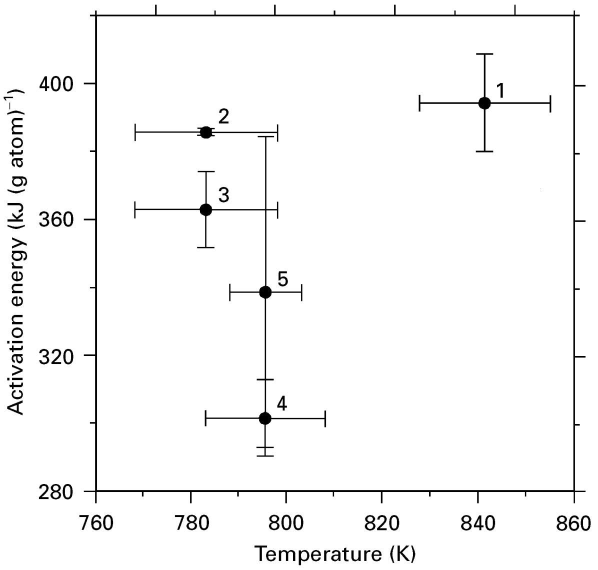

Figure 12 The same as in Fig. 11 for the second crystallization stage, R2, in the as-quenched $Fe_{75}Si_{15}B_{10}$ glassy ribbon. (1) The Kissinger activation energy, E_K^*, (2) and (3) the activation energy calculated from the temperature dependence of the isothermal peak maximum and end time, E_{tm}^* and E_e^*, respectively, (4) the isoconversional isothermal activation energy, E_{Ti}^*, (5) the isothermal Suriñach method activation energy, E_S^*. Horizontal bars – the width of the temperature interval taken into account; vertical bars – the error of the presented mean value.

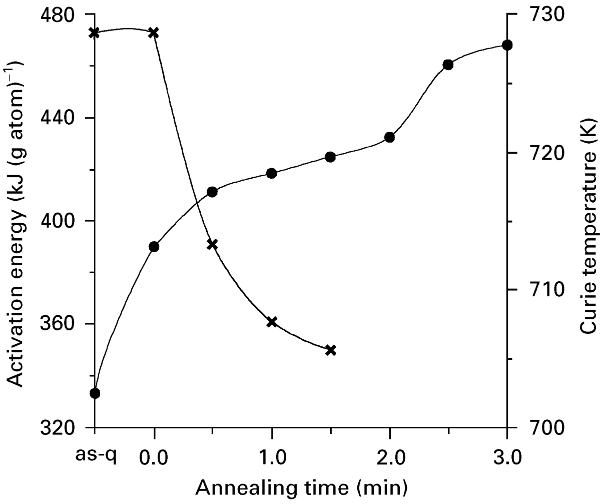

Figure 13 The dependence of the Kissinger activation energy, E_{K1}^* on the pre-annealing time, of the R1 crystallization stage (×) and the Curie temperature of the remaining amorphous matrix, $T_{c,a}$ (●) of the glassy $Fe_{75}Si_{15}B_{10}$ ribbon. (Heating rate 10 K min^{-1}.) Pre-annealing temperature T_a = 793 K [12].

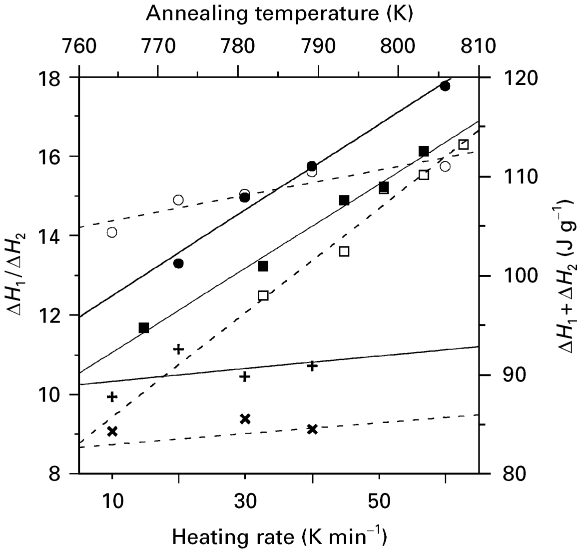

Figure 14 Ratio of the partial crystallization peak enthalpies, (Δ_1H/Δ_2H), and the total crystallization enthalpy, ($\Delta_1H + \Delta_2H$), as a function of the DSC heating rate, φ, or the isothermal crystallization temperature, T_a, of the as-quenched (circles and squares) and heat treated at T_a = 793 K for t_a = 1.5 min (+ and ×) glassy $Fe_{75}Si_{15}B_{10}$ ribbon. Isothermal measurements: ■ (Δ_1H/Δ_2H), □ ($\Delta_1H + \Delta_2H$). Linear-heating measurements: ● and + (Δ_1H/Δ_2H), ○ and × ($\Delta_1H + \Delta_2H$).

crystallization stage of the as-quenched $Fe_{75}Si_{15}B_{10}$ ribbon. However, after appropriate heat treatment of the sample (e.g. pre-annealing at a temperature T_a activating the R1 crystallization stage, as indicated in Fig. 3 for the isothermal DSC curve for T_a = 793 K), the decrease of $E_1^*(t_a)$ can be observed (Fig. 13). Simultaneously, the Curie temperature of the remaining amorphous matrix $T_{c,a}(t_a)$ has a tendency to saturate followed by a steep increase for the prolonged pre-annealing times t_a (Fig. 13). On the other hand, the dynamics both of $E_1^*(\alpha)$ and $n_1(\alpha)$ decays. Finally, E_1^* has a value of ~350 kJ (g atom)$^{-1}$ and n_1 remains at only 1.5 for the whole R1 stage (Figs 9 and 10a in [12]). (By contrast, structural relaxation does not affect E_1^* but increases $T_{c,a}$, for a short t_a.)

By contrast, no change in the kinetics of the second transformation step R2 was indicated (Figs 5 and 6b). $E_2^* \sim 330$ kJ (g atom)$^{-1}$ $\neq f(\alpha)$ and $n_2 = 3 \neq f(\alpha)$. However, as the Kissinger plot based on the dynamic DSC measurements did not give a straight line (Fig. 4), the temperature dependence of the R2 processes, $E_2^* = f(T)$, can be guessed. Moreover, the shape of the DSC transformation curves is dependent on the parameters of the measuring regime such as the annealing temperature, T_a and the heating rate, φ, both in the isothermal and dynamic measurements. Namely, as shown in Fig. 14, the ratio of the enthalpies of the two peaks $\Delta H_1/\Delta H_2$ and also the total enthalpy of the whole crystallization $\Delta H_1 + \Delta H_2$ increase continuously with T_a or φ in the as-quenched samples whereas they remain constant in the well pre-annealed, e.g. pre-crystallized samples. This suggests that the R1 crystallization step is temperature dependent. As the kinetics of R1 were found to be independent of T, probably its starting condition, i.e. the early stages of nucleation or alternatively pre-nucleation of the primary phases, must be controlled by T. Thus, the relative proportions of the transforming phases in the R2 stage are modified and the apparent activation energy, $E_2^* = f(T)$, reflects the previously mentioned temperature dependence of R1. Actually, $E_2^*(T_a)$ calculated by the Suriñach method significantly decreases with increasing T_a. This dependence results in a larger uncertainty of the mean value of E_{S2}^* shown in Fig. 12. Consequently, E_{Ti2}^* calculated by the isoconversional isothermal method, reaches an unrealistic low absolute value. However, the increase of the effective value of $E_{K2}^*(T)$ with φ reflects a phenomenon opposite to the isothermal T_a dependence discussed, namely a shortening of the accessible R1 nucleation time.

4.2. Crystallization mechanism

According to the structural and kinetic investigation of the crystallization process in the $Fe_{75}Si_{15}B_{10}$ ribbon the first reaction R1 represents the nucleation and diffusion controlled 3-dimensional growth of two types of crystals—α-Fe(Si)/Fe_3Si—regions and composites consisting of orthorhombic Fe_3B cores surrounded by α-Fe(Si)—within the amorphous matrix. At first, the homogeneously nucleated α-Fe(Si) crystals prevail until the Fe_3B cores achieve sufficient size to become the centres for the heterogeneous nucleation of α-Fe(Si). The rate of growth of the composites is higher than that of the homogeneously nucleated α-Fe(Si) single crystals. Later, when $\alpha > 0.6$ and the heterogeneous nucleation of the composites becomes exhausted, the growth prevails in the complex R1 transformation. The controlling role of the growth of the α-Fe(Si) and Fe_3Si crystals in the R1 crystallization stage is supported also by the steep increase of the ferromagnetic Curie temperature of the remaining amorphous matrix $T_{c,a}$ with increasing content of the R1 crystallization product, α_1, (which is related to the pre-annealing time) (Fig. 13).

The remaining amorphous matrix crystallizes by a eutectic reaction during the second stage of the crystallization forming a $Fe_3Si + Fe_2B$ eutectic structure. Though $E_2^* < E_1^*$, the R2 transformation cannot start until the matrix achieves an appropriate chemical composition. The relatively large metastable Fe_3B cores of the composites also transform into the finer stable Fe_2B microcrystals by a eutectic decomposition reaction during the R2 stage.

Because both $R1 = f(\alpha)$ and $R2 = f(T)$ crystallization stages were found to be complex transformations of more than one phase, the activation energies determined by DSC depend on the method of kinetic analysis used (see Figs 11 and 12) and their physical significance is doubtful. However, such observations are frequent in the context of devitrification of metallic glasses, namely in all Fe–Si–B glasses [4, 6–9, 12, 13]. The high absolute values of activation energies (also in [4, 6–9, 12, 13]) suggest the mechanisms of cooperative motions of larger structural units (the structure of which could not be determined by our experimental techniques) rather than the jumps of single atoms.

The $Fe_{75}Si_{15}B_{10}$ alloy studied is hypereutectic and lies very close to the pseudobinary eutectic trough [9]. Therefore, the primary crystallization of Fe_3B in the amorphous ribbons was expected as mentioned in the introduction. In this study both supersaturated solid solution α-Fe(Si) and ordered DO_3 Fe_3Si reflections were also present in both the TEM and X-rays diffraction patterns. This may reflect the width of the eutectic trough where both types of primary crystals may form in the R1 crystallization stage. The reliability of the reported projection of the eutectic lines in the ternary diagram may also be questioned with respect to the non-equilibrium thermodynamic state of the studied alloy (e.g. there is a difference between the pseudobinary lines in the case of the Fe–Si–B ternary diagrams reported in references [9] and [3]).

The formation of the primary Fe_3B microcrystals, and especially their number and critical dimensions to become the cores of the composites, are probably the parameters which control not only the relative proportions of the R1 and R2 products but also the chemical composition of the latter. Therefore while n_2 remains constant, $E_2^*(T)$ follows the changes in the chemical composition of the eutectics. This hypothesis is supported by Gibson and Delamore [5] who also observed a heating rate dependence of the shapes of the dynamic DSC curves for several hypereutectic Fe–Si–B metallic glass ribbons. In all these ribbons (and only in these cases) composite crystals, having the Fe_3B core as a product of the R1 crystallization step, were detected.

The question as to when and how the Fe_3B microcrystals are formed, has not been answered so far and it will be the subject of future studies.

While in the early stage of the R1 transformation the metastable Fe_3B phase appeared, the stable Fe_2B phase was observed in the completely crystallized ribbons. Taking into account the large heat effects of the R1 and R2 crystallization stages, the kinetics of the simultaneous Fe_3B to Fe_2B transformation could not be determined by any DSC experiment.

5. Conclusions

Two large exothermic peaks at 831 and 848 K (referred to as the R1 and R2 peaks), the first being more than 10 times larger than the second, and the accompanying fine structure of the DSC curve for the glassy $Fe_{75}Si_{15}B_{10}$ ribbon were observed. Extensive DSC, TM, TEM and X-ray measurements were carried out for the as-quenched and pre-annealed samples in order to discuss the origin of these peaks. The annealing temperatures were chosen to characterize the crystallization stages R1 and R2 that appeared in the DSC curves of the as-quenched samples.

The R1 peak was attributed to the crystallization of two types of microcrystals. The first type is the homogeneously nucleating and growing b.c.c. α-Fe supersaturated with 20 at % of Si and Fe_3Si with the DO_3 symmetry, alternatively. The second type are the composite crystals, which consist of b.c.c. α-Fe nucleating heterogeneously and growing on the surface of the previously formed orthorhombic Fe_3B microcrystalline cores. The presence of Fe_3Si in the second type of the primary crystals was not directly detected. The relative proportions of these two types of microcrystals are dependent on the temperature. The decay of the nucleation and the three-dimensional diffusion-controlled growth of the composite are the prevailing mechanisms in the advanced stages of the R1 transformation (for $\alpha_1 > 0.6$).

During the primary crystallization of the amorphous ribbon, the chemical composition of the matrix continuously changes to reach the eutectic one. Finally, following the R2 peak, the remaining amorphous matrix crystallizes by the eutectic reaction forming the

Fe_3Si and Fe_2B eutectic structure. Simultaneously, the primary metastable Fe_3B cores of the composites also transform into the stable Fe_2B microcrystals.

The kinetics of the R1 and R2 DSC peaks was studied by the Kissinger, isoconversional and Suriñach curve fitting procedures. All the isothermally and dynamically measured data of both DSC peaks are characterized by the JMA nucleation-and-growth kinetics. The apparent activation energy of the primary crystallization, $E_1^* = f(\alpha_1)$, decreases with increasing α_1 during R1 and with the pre-annealing promoting the formation of the Fe_3B cores. E_1^* of the α-Fe(Si) growth in the already nucleated sample is $350\ \mathrm{kJ\,(g\,atom)^{-1}}$ and the JMA exponent $n_1 = 1.5$. $E_1^* = 480\ \mathrm{kJ\,(g\,atom)^{-1}}$ and $n_1 = 2.5$ for $\alpha < 0.6$ in the case of the as-quenched sample. Both E_1^* and n_1 are independent of temperature. The apparent activation energy of the eutectic reaction, $E_2^* = f(T)$, decreases from 384 to $292\ \mathrm{kJ\,(g\,atom)^{-1}}$ with increasing temperature of the R1 reaction. Simultaneously, the content of boron in the crystallizing pseudobinary eutectics decreases. The parameters E_2^* and $n_2 = 3$ are constant during the R2 transformation.

References

1. A. DATTA, N. J. DECRISTOFARO and L. A. DAVIS, Proceedings of the Fourth International Conference on Rapidly Quenched Metals, Japan (1981) edited by J. Masumoto and X. Suzuki, p. 1007.
2. Y. YOSHIZAWA, S. OGUMA and K. YAMAGUCHI, *J. Appl. Phys.* **64** (1988) 6044; Y. YOSHIZAWA, K. YAMAGUCHI, T. YAMANE and H. SUGIHARA, *J. Appl. Phys.* **64** (1988) 6047.
3. M. A. GIBSON and G. W. DELAMORE, *Mater. Sci. Eng. A* **117** (1989) 255.
4. M. A. GIBSON and G. W. DELAMORE, *Acta Metall. Mater.* **38** (1990) 2621.
5. M. A. GIBSON and G. W. DELAMORE, *J. Mater. Sci.* **27** (1992) 3533.
6. E. ILLEKOVÁ, *Thermochimica Acta* **280/281** (1996) 289.
7. E. ILLEKOVÁ, F. MALIZIA and F. RONCONI, *ibid.* **282/283** (1996) 91.
8. I. MAT'KO, E. ILLEKOVÁ, P. DUHAJ, P. ŠVEC, *Mater. Sci. Eng. A* (in press).
9. V. R. V. RAMANAN and G. E. FISH, *J. Appl. Phys.* **53** (1982) 2273.
10. H. E. KISSINGER, *Anal. Chem.* **29** (1957) 1702.
11. S. SURIÑACH, M. D. BARO, M. T. CLAVAGUERA-MORA and N CLAVAGUERA, *J. Non-Cryst. Solids* **58** (1983) 209.
12. E. ILLEKOVÁ, F. A. KUHNAST, I. MAT'KO and Ch. NAGUET, *Mater. Sci. Eng. A* **215** (1996) 150.
13. E. ILLEKOVÁ, K. CZOMOROVÁ, F. A. KUHNAST, J. M. FIORANI, *ibid. A* **205** (1996) 166.
14. G. INDEN, *Bull. Alloy Phase Diagrams* **2** (1982) 412.

Received 8 January 1996
and accepted 11 February 1997